

Sulfur-Tolerant Hierarchically Porous Ceramic Anode-Supported Solid-Oxide Fuel Cells with Self-Precipitated Nanocatalyst

Yu Chen,^[a] Yanxiang Zhang,^[a, b] Guoliang Xiao,^[a] Zhibin Yang,^[c] Minfang Han,^{*[c, d]} and Fanglin Chen^{*[a]}

A hierarchically porous $\text{Sr}_2\text{Fe}_{1.5}\text{Mo}_{0.5}\text{O}_{6-\delta}-\text{Gd}_{0.1}\text{Ce}_{0.9}\text{O}_{1.95}$ (SFM-GDC) ceramic anode-supported solid-oxide fuel cell with a GDC electrolyte film was fabricated by freeze-drying tape-casting and drop coating. 3D X-ray computed tomography analysis indicated that the SFM-GDC anode has a high porosity and low tortuosity factor, facilitating gas diffusion in the anode during fuel cell operation. Peak power density of cells with a $\text{La}_{0.6}\text{Sr}_{0.4}\text{Co}_{0.2}\text{Fe}_{0.8}\text{O}_3$ -GDC (LSCF-GDC) cathode can reach 0.22 W cm^{-2} at 700°C when using H_2 as the fuel and ambient

air as the oxidant. The SFM-GDC anode shows excellent sulfur tolerance when using H_2 with 50 ppm H_2S . SEM analysis demonstrates that the nanocatalyst (iron) can precipitate from the parent SFM phase upon reduction and iron nanoparticles can react with sulfur species to form needle-like nanosulfide. Both the nanocatalyst and sulfide show a graded distribution along the thickness direction, owing to a graded local oxygen chemical potential within the anode.

1. Introduction

A solid-oxide fuel cell (SOFC) is an energy-conversion device that can directly convert the chemical energy in a fuel into electricity with advantages such as high efficiency, low pollution, and fuel flexibility.^[1] The current generation of SOFCs is based on an anode-supported cell configuration, using Ni-based cermet anodes.^[2] In such a cell design, a thick anode substrate and thin electrolyte can be co-sintered to achieve good interlocking between the anode and electrolyte.^[3] Such a Ni-based anode-supported SOFC can produce a high cell power output, owing to the low ohmic losses, with a thin electrolyte membrane and sufficient porosity achievable for both the anode and cathode.^[4]

One distinguishing advantage of SOFCs that use oxide-conducting electrolytes is that, in principle, they are able to convert the energy stored in any hydrocarbon fuel directly into electricity. However, sulfur species in the available hydrocarbon

fuels will unfavorably react with the Ni catalyst in a conventional nickel-yttrium-stabilized zirconia (Ni-YSZ) anode, resulting in severe anode sulfur poisoning and, thus, significant cell performance loss.^[5] In addition, Ni-based anodes suffer from instability upon redox cycling.^[6] Ceramic anodes such as $\text{La}_{0.75}\text{Sr}_{0.25}\text{Cr}_{0.5}\text{Mn}_{0.5}\text{O}_3$,^[7] $\text{Sr}_2\text{Mg}_{1-x}\text{Mn}_x\text{MoO}_6$,^[8] or La-doped SrTiO_3 ,^[9] have been explored to replace Ni-based cermet anodes, despite their low electrical conductivity and inadequate catalytic activity. To enhance the electrochemical/catalytic activity of ceramic electrodes, additional catalyst coatings have generally been applied through infiltration.^[10] In addition to conventional deposition methods, perovskite materials that can self-extract nanocatalysts may enhance catalytic activity during fuel-cell operation, which become more attractive for the simplicity.^[11]

Recently, we discovered a novel double-perovskite material $\text{Sr}_2\text{Fe}_{2-x}\text{Mo}_x\text{O}_3$ as a SOFC anode, thereby combining high electrical conductivity, electrocatalytic activity, and redox stability.^[12] Cells that use such perovskite-based anodes are normally designed with an electrolyte-supported configuration. As there are significant ohmic losses from the electrolyte, the cell performance is typically low for a cell with ceramic anodes, even when a highly conducting electrolyte such as $\text{La}_{0.9}\text{Sr}_{0.1}\text{Ga}_{0.8}\text{Mg}_{0.2}\text{O}_3$ is used.^[12a] Therefore, it is of great significance to develop perovskite-based anode-supported SOFCs to decrease ohmic losses as well as to maximize the sulfur tolerance. However, it is challenging to fabricate high-performance ceramic anode-supported cells. It is extremely difficult to achieve the required porosity and tortuosity factor in the anode, as a high-temperature sintering process is needed to densify the electrolyte membrane, but the ceramic anode also densifies under such sintering conditions. The low porosity and high

[a] Dr. Y. Chen, Dr. Y. Zhang, Dr. G. Xiao, Prof. F. Chen

Department of Mechanical Engineering

University of South Carolina

300 Main Street, Columbia, SC 29208 (USA)

E-mail: chenfa@cec.sc.edu

[b] Dr. Y. Zhang

National Key Laboratory for Precision Hot Processing of Metals

School of Materials Science and Engineering

Harbin Institute of Technology, Harbin

Heilongjiang 150001 (China)

[c] Dr. Z. Yang, Prof. M. Han

School of Chemical & Environment Engineering

China University of Mining & Technology

Beijing, 100083 (China)

[d] Prof. M. Han

Department of Thermal Engineering

Tsinghua University, Beijing, 100084 (China)

E-mail: hanminfang@sina.com

tortuosity factor will increase the gas-diffusion resistance.^[13] Freeze-drying tape-casting processes can overcome the above-mentioned challenges and produce an electrode substrate with open and straight gas-diffusion channels (5–200 µm) with high shrinkage levels after high-temperature sintering.^[14]

In this study, hierarchically porous $\text{Sr}_2\text{Fe}_{1.5}\text{Mo}_{0.5}\text{O}_{6-\delta}$ – $\text{Gd}_{0.1}\text{Ce}_{0.9}\text{O}_{1.95}$ (SFM–GDC) (50:50 mass ratio) ceramic anode-supported SOFCs with a GDC electrolyte film were fabricated by using a combination of freeze-drying tape-casting and drop-coating. The microstructure of the anode substrate and single cell after electrochemical measurement was examined by either scanning electron microscope (SEM) or 3D X-ray mi-

croscopy. The porosity, tortuosity factor, and 3D microstructure of the anode substrate were determined and reconstructed by using Matlab code. The cell performance when using H_2 and H_2 with 50 ppm H_2S as the fuel is evaluated.

2. Results and Discussion

Figure 1 shows the microstructure information for the SFM–GDC anode support sintered at 1400 °C for 5 h, which was fabricated by freeze-drying tape-casting. The open and straight pores are generated by the removal/sublimation of ice crystals during the freeze-drying process. In the freeze tape-casting

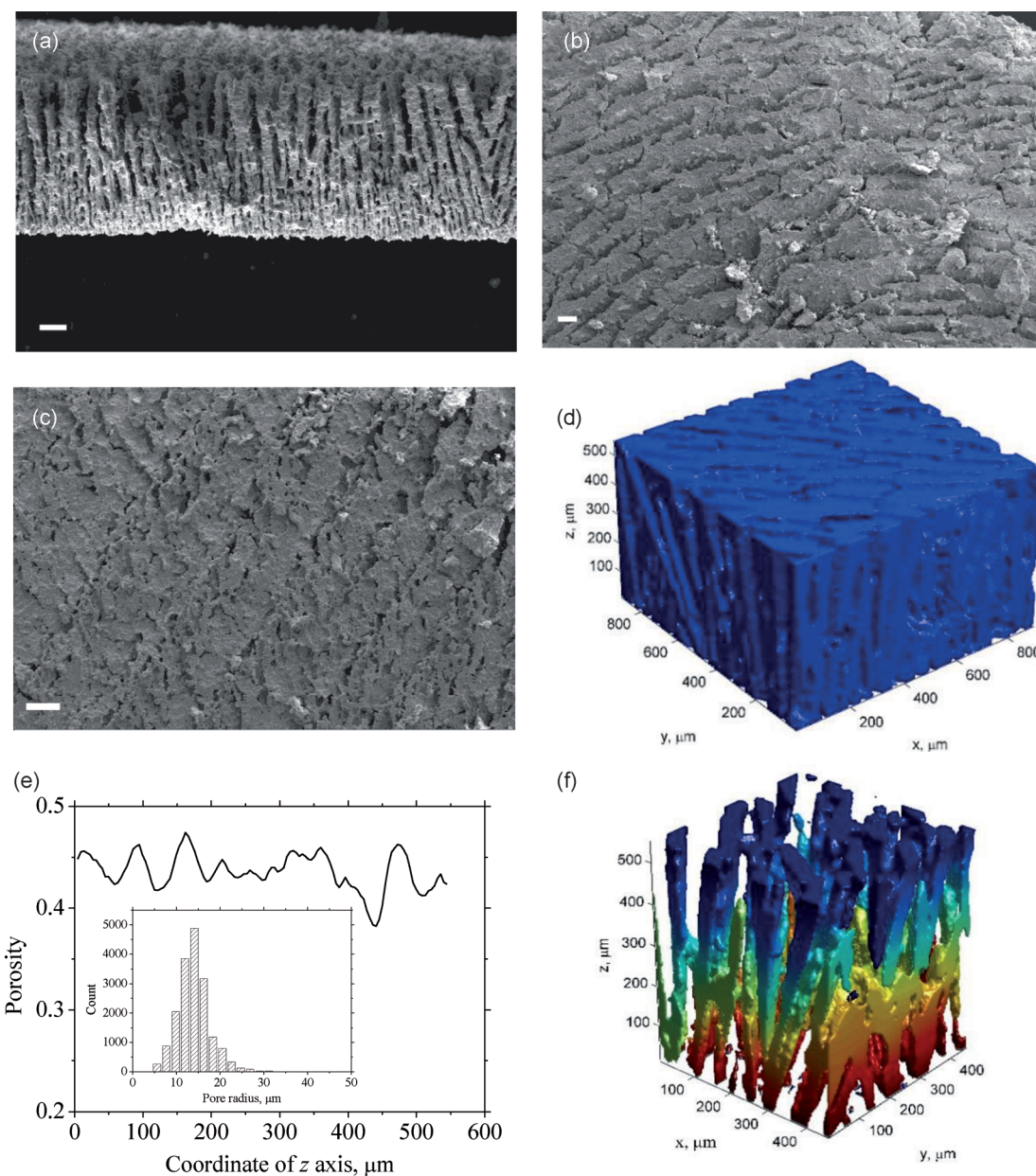


Figure 1. a) A typical cross-sectional SEM image for the SFM–GDC anode substrate and b) bottom and c) top surface view of the same anode substrate; the scale bar in (a–c) is 100 µm. d) Reconstructed 3D microstructure images of the SFM–GDC anode substrate e) distribution of the local porosity along z axis for the reconstructed 3D images, and f) visualization of a general field within the porous channels of the SFM–GDC substrate when the field is conducted along the thickness direction. Colors from red to blue proportionally represent high to low field potential. Inset of (e) is the pore radius distribution of the SFM–GDC anode substrate.

stage, water was first frozen and nucleated on the Mylar film (-70°C) and then grown upwards along the temperature gradient, causing the ice crystals to diverge, finally resulting in a less tortuous structure.^[15] Figure 1a shows the cross-sectional SEM view of the SFM-GDC anode substrate, which is similar to our previous results.^[14a] The bottom surface of substrate is the area close to the Mylar polymer film on the casting bed, where ice nucleation started. The top surface is the area far from the Mylar film, exposed to ambient air during freeze tape-casting. Figure 1b and Figure 1c show the bottom and top surface SEM views of the SFM-GDC anode substrate in Figure 1a, respectively. Both the cross-sectional and surface images indicate graded pore/channel size along the thickness direction. Figure 1d shows the reconstructed 3D morphology image obtained by directly stacking the raw X-ray gray images along the x axis in sequence. The interval step between images is $4.53\ \mu\text{m}$, which is the same as the resolution of the images. Figure 1e shows the porosity results, calculated as the fraction of pore pixels in the 2D slice. The porosity is around 43%, which is distributed along the thickness direction, similar to our previous experimental result for the NiO-YSZ substrate (49%).^[14a] The inset of Figure 1e is the pore radius distribution from the SFM-GDC anode substrate, demonstrating a dominant pore size of $15\ \mu\text{m}$. Figure 1f shows the distribution of a general field (e.g. fuel concentration) within the porous channels of the anode substrate when the field is conducted along the thickness direction. As can be seen, the potential evolved smoothly from the bottom to the top, indicating a low tortuosity for gas diffusion. The tortuosity factor was determined as approximately 1.4. Details about the porosity and tortuosity factor calculation can be found in our previous paper.^[3b] The less tortuous anode substrate is expected to enhance heat and mass transfer and, hence, is of special interest in heterogeneous catalytic processes determined by heat or mass transfer.

Before recording the voltage and current data, the anode of the cells was reduced/polarized at 600°C for 95 h using 3 vol% humidified H_2 under a constant voltage of $0.5\ \text{V}$. Figure 2a shows the cell voltage, current, and power output curves of cells measured at 600 and 700°C when using H_2 as the fuel and ambient air as the oxidant. The cell peak power densities are 0.14 and $0.22\ \text{W cm}^{-2}$ at 600 and 700°C , respectively, which are higher than those reported previously (0.039 and $0.188\ \text{W cm}^{-2}$ at 600 and 700°C).^[16] In the previous study, a traditional tape-casting method was applied for the fabrication of the SFM-GDC anode with a sponge-like microstructure, which may increase the gas-diffusion resistance. However, the cell power output is lower than values reported for other ceramic anode-supported cells with impregnated metal catalysts in the ceramic anode.^[17] The metal infiltrate can increase anode conductivity and improve catalytic activity.^[10a, 17] Figure 2b shows the electrochemical impedance spectra measured at 600 and 700°C for SFM-GDC anode-supported cells under open-circuit voltage conditions when using H_2 as the fuel and ambient air as the oxidant. The ohmic resistance values are 0.41 and $0.24\ \Omega\text{cm}^2$ at 600 and 700°C , respectively. The theoretical ohmic resistance from the GDC electrolyte (ca. $35\ \mu\text{m}$) is calculated as approximately 0.23 and $0.075\ \Omega\text{cm}^2$ at 600 and 700°C ,

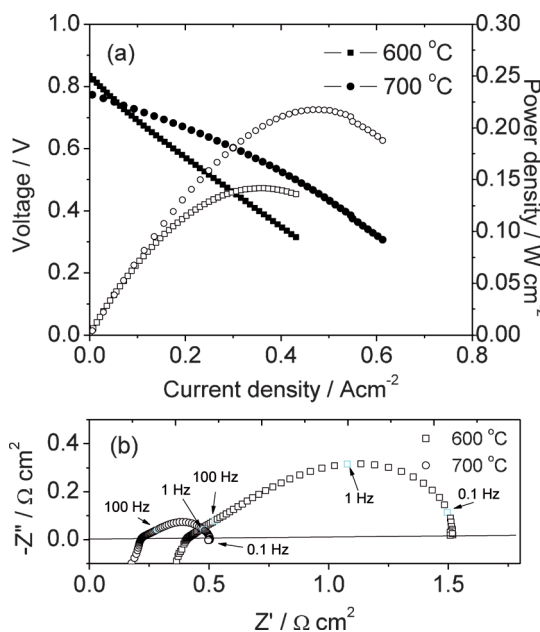


Figure 2. a) Current–voltage and current–power curves of SFM–GDC anode-supported cells measured at different temperatures using H_2 as the fuel and ambient air as the oxidant; b) impedance spectra of cells tested at different temperatures under open-circuit conditions.

respectively (conductivity of GDC at 600 and 700°C is measured to be 0.015 and $0.047\ \text{Scm}^{-1}$, respectively). The difference (0.18 and $0.165\ \Omega\text{cm}^2$ at 600 and 700°C , respectively) can be attributed to the thick, highly porous anode and contact resistances.

Figure 3 shows the bulk electrical conductivity of SFM and SFM-GDC (mass ratio of 1:1) measured under wet H_2 (3 vol% H_2O) conditions. The electrical conductivity of SFM-GDC in H_2 reached $2.5\ \text{Scm}^{-1}$ at 700°C , which is lower than that for SFM ($17.5\ \text{Scm}^{-1}$) in H_2 , owing to the relatively low electrical conductivity of GDC. The theoretical ohmic resistance for a dense SFM-GDC anode ($550\ \mu\text{m}$) can be calculated as $0.022\ \Omega\text{cm}^2$. By considering the high porosity and low tortuosity factor, the actual ohmic resistance from the anode is expected to be higher.

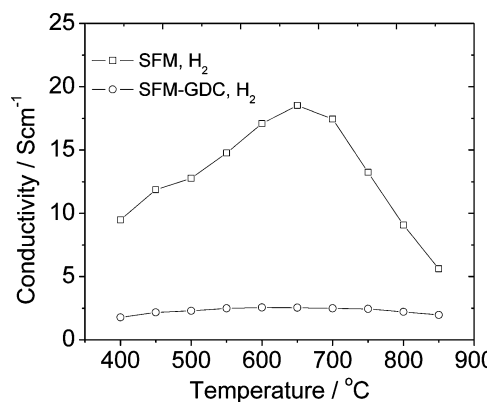


Figure 3. Electrical conductivity of bulk SFM and SFM-GDC.

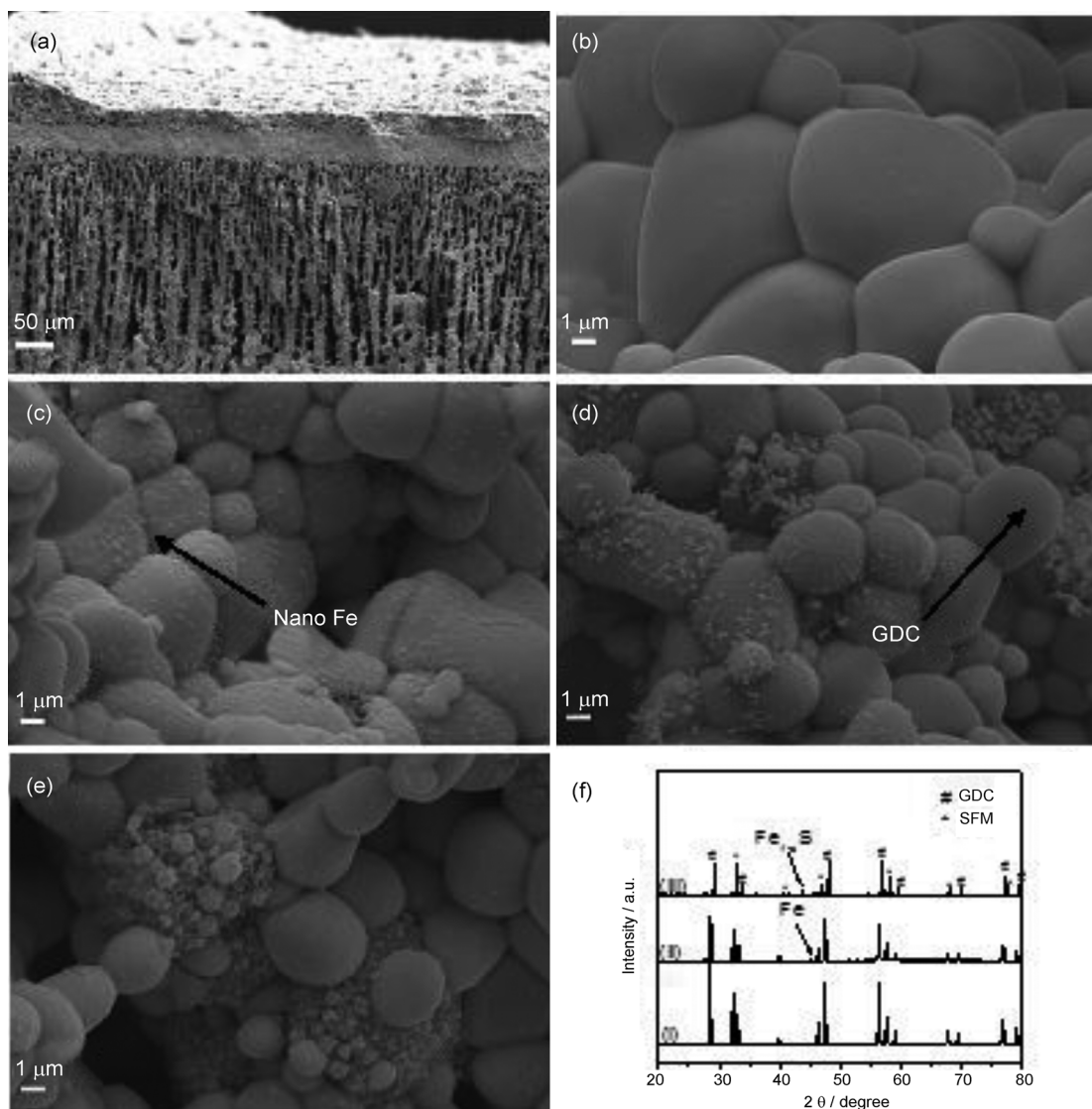


Figure 4. a) SEM image of the cross-sectional view of the SFM–GDC anode-supported cells after fuel-cell measurement; b) SEM image of the anode before fuel-cell measurement; c) SEM image (after fuel-cell measurement) of the area close to the electrolyte (10 μm); d) SEM image (after fuel-cell measurement) of the area far from the electrolyte (100 μm); e) SEM image (after fuel-cell measurement) of the area further away from the electrolyte (400 μm); f) XRD patterns for the SFM–GDC anode: i) before and ii) after measurement with H_2 and iii) after measurement with H_2 containing 50 ppm H_2S .

Figure 4a shows the microstructure of SFM–GDC anode-supported cells after measurement, using H_2 as the fuel for 200 h (under a constant cell voltage of 0.5 V). The dense electrolyte (ca. 35 μm) is well adhered to both the anode (ca. 550 μm) and the cathode (ca. 30 μm). The hierarchically oriented straight pores/channels are expected to facilitate mass transport in the anode. It is interesting to note that nano-sized particles can be observed on the SFM surface, as shown in Figure 4c–e. In addition, the nanoparticles were graded along the thickness direction of the SFM–GDC anode. The nanoparticles close to the electrolyte/anode functional layer are much smaller, whereas the nanoparticles far from the electrolyte are larger. Figure 4b shows the anode particles before electrochemical measurement. Figure 4c shows the nanoparticles about 10 μm from the electrolyte. Figure 4d shows the nanoparticles about 100 μm from the electrolyte. Figure 4e shows the nanoparti-

cles about 400 μm from the electrolyte. The size of the nanoparticles in Figure 4c are in the range of 50–100 nm, that is, they are smaller than those in Figures 4d and e. These nanoparticles were identified to be Fe, as shown in Figure 4f, which exhibits the XRD patterns for the anode substrate before and after electrochemical measurements. The B-site cation is easy to precipitate under reduction conditions, which is consistent with the results reported earlier.^[11e] When perovskite oxides (ABO_3) are employed as supporting skeletons, certain catalysts can be incorporated as cations at the B site of the perovskite lattice under oxidizing conditions and partly exsolved as nanoparticles upon subsequent reduction.^[18]

Figure 5a shows the short-term stability test of the SFM–GDC anode-supported cells at 600 °C under a constant voltage of 0.5 V. The cell performance, using H_2 as the fuel, increased in the first 200 h and then stabilized after operating for anoth-

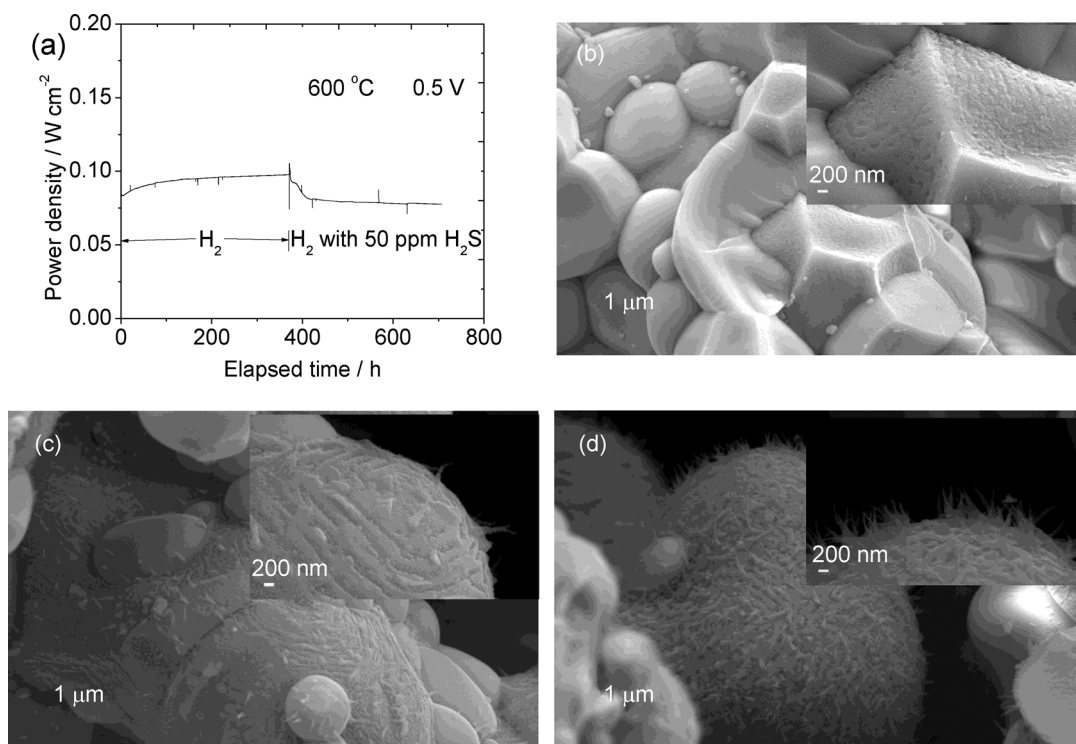


Figure 5. a) Sulfur tolerance test for SFM-GDC anode-supported cells under a constant voltage of 0.5 V at 600°C , using either H_2 or H_2 with 50 ppm H_2S as the fuel and ambient air as the oxidant; b) SEM image (after the sulfur tolerance test) of the area close to the electrolyte (10 μm); c) SEM image (after the sulfur tolerance test) of the area far from the electrolyte (100 μm) and d) SEM image (after the sulfur tolerance test) of the area further away from the electrolyte (400 μm).

er 200 h. The initial increase in cell output can probably be attributed to either the precipitation of Fe nanoparticles or the activation of electrodes. Fe nanoparticles may increase the conductivity or catalytic activity of the anode. After switching the fuel from H_2 to H_2 with 50 ppm H_2S , the cell suffers from a fast degradation in the first 46 h, which may be attributed to catalyst deactivation by sulfur poisoning. However, the cell showed a stable performance in the subsequent 300 h of operation, using H_2 with 50 ppm H_2S as the fuel. The excellent sulfur tolerance of SFM-GDC is consistent with our previous result.^[12b] GDC in the anode can function as a sulfur absorbent that can be regenerated.^[19] In addition, we found a similar size trend for the needle-like structure as for the Fe nanoparticles along the anode thickness direction, as shown in Figures 5 b, c, and d. The needle-like structure was determined as Fe_{1-x}S (PDF# 17-0211), according to the XRD pattern shown in Figure 4 f. Very few needle-like sulfide structures can be found in the anode functional layer (Figure 5 b, 10 μm from the electrolyte). More and longer needle-like sulfides can be observed when you look further away from the electrolyte (Figures 5 c and d show images obtained 100 and 400 μm from the electrolyte, respectively). The formation of sulfide can protect the anode by attracting or absorbing H_2S to react with the nanocatalyst instead of the parent matrix (Fe-deficient SFM). SFM is also an excellent oxygen-ion conductor, which may provide an oxygen flux during fuel cell operation, facilitating the removal of sulfide. The excellent stability may be attributed to the equilibrium between the sulfide formation and removal.

It is well accepted that fuel oxidation occurred at the triple-phase boundary sites, mostly in the area 10 μm adjacent to the electrolyte, which is the so-called anode functional layer.^[20] The anodic polarization of the SFM-GDC anode induces a graded distribution of oxygen chemical potential (μ_{O_2}) or a graded-oxygen stoichiometric number in the perovskite along the thickness direction of the anode. In other words, the μ_{O_2} in the vicinity of the anode/electrolyte interface is higher than that in the anode bulk. This may be the reason why the size of either the Fe nanoparticles or the sulfide increases gradually along the thickness direction of the anode. The oxygen species in the high- μ_{O_2} layer is expected to hinder the reduction of perovskite or precipitation of the B-site metal, and accelerate the removal of sulfur species. The balance between sulfide removal and formation in the anode functional layer (10 μm from the electrolyte) is suggested to be one of the possible reasons for the excellent sulfur tolerance.

3. Conclusions

Hierarchically porous SFM-GDC anode-supported SOFCs were fabricated through a combination of freeze drying tape-casting and co-sintering. The freeze-drying tape-casting allowed the fabrication of highly porous ceramic anode substrate, enabling the fabrication of a dense electrolyte film through high-temperature sintering. The microstructure of the SFM-GDC anode substrate was studied and reconstructed three dimensionally. The porosity distribution, pore size distribution, and tortuosity

factor were determined quantitatively from the 3D reconstruction and subsequent calculation. SFM–GDC anode-supported cells with a GDC electrolyte film and a $\text{La}_{0.6}\text{Sr}_{0.4}\text{Co}_{0.2}\text{Fe}_{0.8}\text{O}_3$ –GDC (LSCF–GDC) cathode show a power density of 0.14 and 0.22 W cm^{-2} at 600 and 700°C , respectively, when using H_2 as the fuel and ambient air as the oxidant. In addition, the SFM–GDC anode shows excellent sulfur tolerance. After the stability test in H_2 and H_2 with 50 ppm H_2S , iron nanoparticles precipitated from the parent SFM and sulfide species were found to be gradually distributed along the anode thickness direction, probably caused by the graded oxygen partial pressure along the thickness direction, accounting for the excellent sulfur tolerance.

Experimental Section

$\text{Sr}_2\text{Fe}_{1.5}\text{Mo}_{0.5}\text{O}_6$ (SFM) powders were prepared by using the solution combustion method^[12b] and were pre-sintered at 1400°C for 2 h before mixing with $\text{Gd}_{0.1}\text{Ce}_{0.9}\text{O}_2$ (GDC). GDC and $\text{La}_{0.6}\text{Sr}_{0.4}\text{Co}_{0.2}\text{Fe}_{0.8}\text{O}_3$ (LSCF) powders were purchased from Fuel Cell Materials (USA). The SFM–GDC (mass ratio of 1:1) anode substrate was prepared by a freeze-drying tape-casting process, as reported in our previous studies.^[14a,21] A GDC electrolyte slurry was directly deposited on the green SFM–GDC anode substrate through a drop-coating process.^[22] The electrolyte/anode bilayer was then sintered at 1400°C for 12 h at a heating rate of 1°C min^{-1} up to 600°C and then heated at 2°C min^{-1} above 600°C . The LSCF–GDC (mass ratio of 1:1) cathode with an active area of 0.33 cm^2 was prepared on the GDC electrolyte surface by brushing the LSCF–GDC paste on the GDC electrolyte surface and then heating at 1050°C for 2 h.

The microstructure of SFM–GDC substrate was characterized through both scanning electron microscopy (SEM, Zeiss Ultra plus FESEM) and 3D X-ray microscopy (MicroXCT-400). In-house Matlab code was developed to calculate the porosity along the thickness direction and the tortuosity factor of the anode substrate. XRD patterns of the SFM–GDC anode before and after electrochemical measurement were recorded by using a D/MAX-3C X-ray diffractometer with graphite-monochromatized $\text{CuK}\alpha$ radiation ($\lambda = 1.5418 \text{ \AA}$). Hydrogen (with 3 vol % H_2O) was used as the fuel and ambient air was used as the oxidant. SFM and GDC powders were also mixed and pressed into a rectangular bar ($40 \times 6 \times 2 \text{ mm}^3$) and sintered at 1400°C for 5 h for electrical conductivity measurements. A silver paste was used to attach four Ag probes to the sintered SFM–GDC bar sample. The bar with the Ag wires and paste was placed in a tubular furnace with flowing air or wet H_2 (3 vol % H_2O) at 40 sccm with a mass-flow controller (APEX Alicat Scientific). The resistance was recorded by using a multimeter (Keithley model 2001 7-1/2 DDM) in a dc four-probe configuration from 850 to 400°C . For the conductivity measurements in H_2 , the SFM–GDC bar was first reduced at 800°C for 10 h prior to the conductivity measurement. The H_2 flow rate for fuel-cell testing was controlled at 40 sccm. The current density–voltage curves as well as electrochemical impedance spectra of single cells were measured with a four-probe method by using a multichannel Versa STAT (Princeton Applied Research) at operating temperatures of 600 and 700°C . The impedance of the cells was measured under an open-circuit voltage over a frequency range of 1 MHz to 0.01 Hz. The ohmic resistance was determined from the high-frequency intercept of the impedance spectra with the real axis, whereas the cell interfacial polarization resistance (R_p) was determined from the dif-

ference between the low- and high-frequency intercepts of the impedance spectra with the real axis in the Nyquist plot.

Acknowledgements

We are grateful for the financial support from the U.S. National Science Foundation (DMR-1210792), the 973 Project (2012CB215404), and the NSFC (51261120378).

Keywords: ceramic anode substrate • fuel cells • heterogeneous catalysis • nanostructures • sulfur tolerance

- [1] a) S. C. Singhal, *Solid State Ionics* **2002**, *152*–*153*, 405–410; b) D. Ding, X. Li, S. Y. Lai, K. Gerdes, M. Liu, *Energy Environ. Sci.* **2014**, *7*, 552–575; c) F. Liang, W. Zhou, Z. Zhu, *ChemElectroChem* **2014**, *1*, 1627–1631.
- [2] S. Singhal, K. Kendall, *High-temperature Solid Oxide Fuel Cells: Fundamentals, Design and Applications*, Elsevier, Oxford, **2003**.
- [3] a) R. P. O’Hayre, S.-W. Cha, W. Coletta, F. B. Prinz, *Fuel cell fundamentals*, John Wiley & Sons, New York, **2006**; b) Y. Chen, Y. Zhang, J. Baker, P. Majumdar, Z. Yang, M. Han, F. Chen, *ACS Appl. Mater. Interfaces* **2014**, *6*, 5130–5136.
- [4] a) T. Suzuki, Z. Hasan, Y. Funahashi, T. Yamaguchi, Y. Fujishiro, M. Awano, *Science* **2009**, *325*, 852–855; b) Z. Shao, S. M. Haile, *Nature* **2004**, *431*, 170–173.
- [5] M. Gong, X. Liu, J. Trembly, C. Johnson, *J. Power Sources* **2007**, *168*, 289–298.
- [6] a) J. Malzbender, R. W. Steinbrech, *J. Power Sources* **2007**, *173*, 60–67; b) G. Xiao, F. Chen, *Front. Energy Res.* **2014**, *2*, 181.
- [7] S. Tao, J. T. S. Irvine, *Nat. Mater.* **2003**, *2*, 320–323.
- [8] Y. Huang, R. I. Dass, Z. Xing, J. B. Goodenough, *Science* **2006**, *312*, 254–257.
- [9] J. C. Ruiz-Morales, J. Canales-Vázquez, C. Savaniu, D. Marrero-López, W. Zhou, J. T. S. Irvine, *Nature* **2006**, *439*, 568–571.
- [10] a) G. Xiao, F. Chen, *Electrochem. Commun.* **2011**, *13*, 57–59; b) X. Zhu, Z. Lü, B. Wei, X. Huang, Y. Zhang, W. Su, *J. Power Sources* **2011**, *196*, 729–733; c) D. Ding, M. Liu, Z. Liu, X. Li, K. Blinn, X. Zhu, M. Liu, *Adv. Energy Mater.* **2013**, *3*, 1149–1154.
- [11] a) B. D. Madsen, W. Kobsiriphat, Y. Wang, L. D. Marks, S. A. Barnett, *J. Power Sources* **2007**, *166*, 64–67; b) W. Kobsiriphat, B. D. Madsen, Y. Wang, M. Shah, L. D. Marks, S. A. Barnett, *J. Electrochem. Soc.* **2010**, *157*, B279–B284; c) S. Boulfrad, M. Cassidy, J. T. S. Irvine, *Solid State Ionics* **2011**, *197*, 37–41; d) D. M. Bierschenk, E. Potter-Nelson, C. Hoel, Y. Liao, L. Marks, K. R. Poeppelmeier, S. A. Barnett, *J. Power Sources* **2011**, *196*, 3089–3094; e) D. Neagu, G. Tsekouras, D. N. Miller, H. Ménard, J. T. S. Irvine, *Nat. Chem.* **2013**, *5*, 916–923; f) G. Xiao, S. Wang, Y. Lin, Z. Yang, M. Han, F. Chen, *J. Electrochem. Soc.* **2014**, *161*, F305–F310; g) C. Yang, Z. Yang, C. Jin, G. Xiao, F. Chen, M. Han, *Adv. Mater.* **2012**, *24*, 1439–1443; h) S. Li, Q. Qin, K. Xie, Y. Wang, Y. Wu, *J. Mater. Chem. A* **2013**, *1*, 8984–8993.
- [12] a) Q. Liu, X. Dong, G. Xiao, F. Zhao, F. Chen, *Adv. Mater.* **2010**, *22*, 5478–5482; b) G. Xiao, Q. Liu, X. Dong, K. Huang, F. Chen, *J. Power Sources* **2010**, *195*, 8071–8074.
- [13] A. V. Virkar, J. Chen, C. W. Tanner, J.-W. Kim, *Solid State Ionics* **2000**, *131*, 189–198.
- [14] a) Y. Chen, J. Bunch, T. Li, Z. Mao, F. Chen, *J. Power Sources* **2012**, *213*, 93–99; b) Y. Chen, Y. Lin, Y. Zhang, S. Wang, D. Su, Z. Yang, M. Han, F. Chen, *Nano Energy* **2014**, *8*, 25–33; c) C. Gaudillere, J. Garcia-Fayos, J. M. Serra, *J. Mater. Chem. A* **2014**, *2*, 3828–3833; d) C. Gaudillere, J. Garcia-Fayos, M. Balaguer, J. M. Serra, *ChemSusChem* **2014**, *7*, 2554–2561; e) Y. Chen, Y. Zhang, Y. Lin, Z. Yang, D. Su, M. Han, F. Chen, *Nano Energy* **2014**, *10*, 1–9.
- [15] S. W. Sofie, *J Am Ceram Soc* **2007**, *90*, 2024–2031.
- [16] Z. Yang, Z. Pang, T. Zhu, Z. Zheng, M. Han, *ECS Trans.* **2013**, *57*, 549–554.
- [17] H. Ding, J. Ge, X. Xue, *Electrochim. Solid-State Lett.* **2012**, *15*, B86–B89.
- [18] Y. Nishihata, J. Mizuki, T. Akao, H. Tanaka, M. Uenishi, M. Kimura, T. Okamoto, N. Hamada, *Nature* **2002**, *418*, 164–167.

- [19] M. Flytzani-Stephanopoulos, M. Sakbodin, Z. Wang, *Science* **2006**, *312*, 1508–1510.
- [20] M. Ni, M. K. H. Leung, D. Y. C. Leung, *J. Power Sources* **2007**, *168*, 369–378.
- [21] Y. Chen, Q. Liu, Z. Yang, F. Chen, M. Han, *RSC Adv.* **2012**, *2*, 12118–12121.
- [22] a) Y. Chen, F. Chen, W. Wang, D. Ding, J. Gao, *J. Power Sources* **2011**, *196*, 4987–4991; b) Y. Chen, J. Bunch, C. Jin, C. Yang, F. Chen, *J. Power Sources* **2012**, *204*, 40–45.

Received: December 4, 2104

Published online on January 29, 2015
